

Vortex streets and honeycomb structures in photodetachment driven by linearly polarized few-cycle laser pulses

F. Cajiao Vélez ^{1,*} Lei Geng ² J. Z. Kamiński ¹ Liang-You Peng,^{2,3,†} and K. Krajewska ^{1,‡}

¹*Institute of Theoretical Physics, Faculty of Physics, University of Warsaw, Pasteura 5, 02-093 Warsaw, Poland*

²*State Key Laboratory for Mesoscopic Physics and Frontiers Science Center for Nano-optoelectronics, School of Physics, Peking University, 100871 Beijing, China*

³*Collaborative Innovation Center of Extreme Optics, Shanxi University, 030006 Taiyuan, China*



(Received 8 July 2020; revised 28 August 2020; accepted 10 September 2020; published 7 October 2020)

Generation of electron vortices in photodetachment driven by linearly polarized laser pulses is demonstrated, both within the strong-field approximation and by numerically solving the time-dependent Schrödinger equation. The sensitivity of the resulting vortex patterns in the momentum distributions of photoelectrons to the laser pulse parameters (including the pulse duration, its intensity, and the carrier-envelope phase) is analyzed. It is shown that, for a nonzero carrier-envelope phase of the driving pulse, vortex structures in the probability amplitude of detachment occur, similar to von Kármán vortex streets in fluid mechanics. In addition, hexagonal regions of high probability (honeycomb patterns) are observed, with vortex-antivortex pairs located at their vertices.

DOI: [10.1103/PhysRevA.102.043102](https://doi.org/10.1103/PhysRevA.102.043102)

I. INTRODUCTION

Vortex formation is a common phenomenon [1]. Its investigations in physics (mostly in aero- and hydrodynamics) were initiated by von Helmholtz [2] and Thomson [3]. In quantum mechanics this concept was studied mainly in the context of superfluidity and superconductivity [4,5]. However, in recent years the topic has become very popular also in other branches of fundamental and applied physics. The corresponding achievements have been described recently in many review articles and books (see, e.g., [6–13] and references therein).

Typically, vortexlike motion is stimulated by forces that have helical structure. For instance, large-scale vortices in the atmosphere (such as tropical cyclones) are generated by the presence of the Coriolis force. In quantum mechanics, for instance, vortexlike motion of probability fluid has been mostly investigated either in magnetic fields [10,14–24] (as the magnetic component of the Lorentz force has a form similar to the Coriolis one) or in circularly polarized laser pulses [25,26]. However, it is well known that vortices can be created by disturbances that do not possess helical structures. A good example is the von Kármán vortex street (see, e.g., [27]) generated in air behind an obstacle, or in water by a paddle moving back and forth in a quasiperiodic motion. Such vortex streets were also predicted in a Bose-Einstein condensate while being caused by an obstacle potential moving at a constant velocity [28–30]. In light of these examples the following question arises: Can vortices caused by linear disturbances also be generated within quantum Schrödinger theory? This is a valid question, as the latter can be formulated in terms of hydrodynamical equations for the flow of

probability fluid [31,32]. In the current paper, we provide the answer to this question while considering photodetachment of H^- ions by linearly polarized laser pulses.

In quantum mechanics, vortex electrons carry orbital angular momentum (OAM) along the axis of propagation [6–13]. They can be generated, for instance, in ionization or detachment driven by circularly polarized laser pulses [25,26], in which case the OAM is transferred from laser photons to electrons. Another physical mechanism of generating vortex electrons, involving ionization by a linearly polarized laser field instead, was investigated in [33]. In this case, however, the electron vorticity depends entirely on the initial electron state and orientation of the target, not on the laser field. This is in contrast to the analysis presented in our paper, where detachment of an s -electron by a linearly polarized laser field leads to the formation of vortex-antivortex pairs and the von Kármán vortex streets.

In light of our paper, it is important to mention the work of Larionov *et al.* [34], where ionization of a two-dimensional hydrogen atom by a few-cycle, flat-top laser pulse was considered. Their treatment, based on perturbation methods and the solution of the time-dependent Schrödinger equation (TDSE), demonstrated that linearly polarized pulses can, in fact, create electron vortices. However, their analysis was limited to studying the magnitude of the probability amplitude of ionization. In contrast, our derivations here are based on the strong-field approximation (SFA) [35–37] for photodetachment, and both the magnitude and the phase of the corresponding probability amplitude are determined. This is necessary to discriminate between vortices and antivortices unmistakably. In addition, we focus here on the influence of laser pulse parameters on the resulting vortex structures in photodetachment. Similarly to Ref. [34], we compare our results with the numerical solution of the TDSE.

As was already described in Ref. [34], the formation of quantum vortices is closely related to destructive interference

*Felipe.Cajiao-Velez@fuw.edu.pl

†liangyou.peng@pku.edu.cn

‡Katarzyna.Krajewska@fuw.edu.pl

effects, since it is necessary that the wave function vanishes at well-defined regions in space for vortices to be present. This is in contrast to fluid mechanics, where the fluid density is always nonzero. We note that the relationship between quantum vortices and destructive interferences was initially studied by Dirac [38] and further developed by Hirschfelder *et al.* [39] (for more information, see, e.g., Ref. [40]). Other modern descriptions of vorticity and interferences driven by linear disturbances, based on the Hamilton-Jakobi formalism, can be found in Refs. [41–43].

This paper is organized as follows. In Sec. II, we describe the main properties of vortex structures arising from the hydrodynamical formulation of quantum mechanics. Such properties are generalized to an arbitrary three-dimensional parametric space in Sec. III. This allows us to analyze the vortex structures in the momentum distribution of photoelectrons. In Sec. IV, we introduce the SFA framework of photodetachment, and we describe briefly the method of solving TDSE. Our model of a laser pulse used in calculations is introduced in Sec. IV B. Section V contains our numerical results. In Sec. V A, we explore the influence of the carrier-envelope phase of the laser pulse on the momentum distribution of photoelectrons and on the formation of vortex structures. The sensitivity of our results to the pulse duration and its intensity are analyzed in Secs. V B and V C, respectively. In Sec. V D we demonstrate how vortices and antivortices in the momentum distributions of photoelectrons may be created (or annihilated). Finally, we present our conclusions and perspectives in Sec. VI.

Unless otherwise stated, we use atomic units (a.u.) for which $\hbar = 1$. However, in our derivations we present the electron charge ($e < 0$) and mass (m_e) explicitly. Some of our numerical illustrations are shown in terms of the atomic unit of momentum, $p_0 = \alpha m_e c$, and the atomic unit of electric field, $\mathcal{E}_{\text{at}} = m_e (\alpha c)^2 / (a_0 |e|)$. Here α is the fine-structure constant, c represents the speed of light (in atomic units $c = 1/\alpha$), and $a_0 = 1/(\alpha m_e c)$ is the Bohr radius.

II. QUANTUM VORTICES

Quantum vortices arise in the hydrodynamical formulation of quantum mechanics, which is due to Madelung [31]. They are associated with the notion of probability fluid, which is described by the density and velocity distributions, $\rho(\mathbf{r}, t)$ and $\mathbf{v}(\mathbf{r}, t)$, respectively. For electrons (of mass m_e) these distributions are defined by the wave function $\psi(\mathbf{r}, t)$,

$$\begin{aligned} \rho(\mathbf{r}, t) &= |\psi(\mathbf{r}, t)|^2, \\ \rho(\mathbf{r}, t) \mathbf{v}(\mathbf{r}, t) &= \frac{1}{m_e} \text{Re}(\psi^*(\mathbf{r}, t) [-i\hbar \nabla] \psi(\mathbf{r}, t)), \end{aligned} \quad (1)$$

and they satisfy the hydrodynamical equations [32,44],

$$\begin{aligned} \partial_t \rho(\mathbf{r}, t) + \nabla \cdot [\rho(\mathbf{r}, t) \mathbf{v}(\mathbf{r}, t)] &= 0, \\ \partial_t \mathbf{v}(\mathbf{r}, t) + [\mathbf{v}(\mathbf{r}, t) \cdot \nabla] \mathbf{v}(\mathbf{r}, t) &= -\frac{\nabla V(\mathbf{r}, t)}{m_e} + \mathbf{f}_Q(\mathbf{r}, t). \end{aligned} \quad (2)$$

Here, $V(\mathbf{r}, t)$ is an external potential whereas $\mathbf{f}_Q(\mathbf{r}, t)$ is the so-called internal quantum force per unit mass,

$$\mathbf{f}_Q(\mathbf{r}, t) = \frac{\hbar^2}{2m_e^2} \nabla \left[\frac{1}{\sqrt{\rho(\mathbf{r}, t)}} \nabla^2 \sqrt{\rho(\mathbf{r}, t)} \right]. \quad (3)$$

Up to now we have kept the Planck constant, so one can see that the force (3) has purely quantum character and vanishes in the limit $\hbar \rightarrow 0$. Hereafter, we set $\hbar = 1$.

The velocity distribution is directly related to the phase of the wave function, $S(\mathbf{r}, t) = \arg[\psi(\mathbf{r}, t)]$ modulo 2π ,

$$\mathbf{v}(\mathbf{r}, t) = \frac{1}{m_e} \nabla S(\mathbf{r}, t). \quad (4)$$

However, the phase $S(\mathbf{r}, t)$ is not uniquely defined at the point \mathbf{r} where the wave function is zero. Note that a vanishing complex wave function results in two separate conditions, $\text{Re}\psi(\mathbf{r}, t) = 0$ and $\text{Im}\psi(\mathbf{r}, t) = 0$, each of them defining a two-dimensional surface in the configuration space. Their intersection can be a surface, a line, or an isolated point. The latter is rather exceptional and we do not encounter such a case in our calculations. When traversing a nodal surface, both the real and imaginary parts of $\psi(\mathbf{r}, t)$ change their sign, which means that the phase of the wave function jumps at the nodal surface by π . Another situation is met at nodal lines (the formation of nodal lines or surfaces and their mapping into different planes are illustrated in Appendix for a particular hydrogen bound-state wave function). Let us consider a closed contour \mathcal{C} that encircles such line. If the line has a vortex character, the phase of the wave function changes from 0 to 2π along the contour \mathcal{C} such that the quantization condition holds,

$$m_e \int_{\mathcal{C}} \mathbf{v}(\mathbf{r}, t) \cdot d\mathbf{r} = 2\pi m, \quad m = \pm 1, \pm 2, \dots, \quad (5)$$

with m called the winding number or the topological charge. It is important to stress that this feature and the resulting condition (5) are valid even when the contour \mathcal{C} approaches the vortex line. In this case, the velocity (4) becomes infinite in order to satisfy Eq. (5). This happens because the phase of the wave function $S(\mathbf{r}, t)$ is singular at vortex points.

In addition, we note that Eq. (5) was determined by Dirac while analyzing the wave function of a charged particle in the presence of electromagnetic fields, close to the nodal points [38]. Most importantly, the vortexlike character of those points can be unambiguously determined only by analyzing the phase of the wave function describing the system. In the next section, we will generalize this description to an arbitrary complex function. This will allow us to analyze vortex structures in the probability amplitude of photodetachment in Sec. V.

III. GENERALIZATIONS

Let us consider a complex function $\mathcal{A}(\mathbf{p})$ that depends on a vector parameter \mathbf{p} . Following the ideas developed originally by Berry [45] (see also Refs. [46–48]), we define the Berry

connection for the phase factor $\mathcal{A}(\mathbf{p})/|\mathcal{A}(\mathbf{p})|$,

$$\begin{aligned} \mathbf{v}(\mathbf{p}) &= \frac{\text{Re}(\mathcal{A}^*(\mathbf{p})[-i\nabla_{\mathbf{p}}]\mathcal{A}(\mathbf{p}))}{|\mathcal{A}(\mathbf{p})|^2} \\ &= \frac{\mathcal{A}^*(\mathbf{p})}{|\mathcal{A}(\mathbf{p})|}[-i\nabla_{\mathbf{p}}]\frac{\mathcal{A}(\mathbf{p})}{|\mathcal{A}(\mathbf{p})|} = \nabla_{\mathbf{p}}(\arg[\mathcal{A}(\mathbf{p})]), \end{aligned} \quad (6)$$

where $\nabla_{\mathbf{p}}$ denotes gradient in the parametric space. This vector-valued function is the analog of the velocity distribution (4) and can be viewed, in light of the Bohm trajectories (see, e.g., Ref. [49]), as an analog of the ratio of momentum to the corresponding mass associated with the function $\mathcal{A}(\mathbf{p})$ defined in an abstract space of parameters \mathbf{p} . That is why we use the same notation, but we distinguish (4) and (6) by their arguments. Similar to the configuration space (see Sec. II), we define a vortex line in the parametric space. Namely, along a vortex line, the function $\mathcal{A}(\mathbf{p})$ vanishes and, for any closed contour \mathcal{C} encircling it, the quantization condition holds,

$$\int_{\mathcal{C}} \mathbf{v}(\mathbf{p}) \cdot d\mathbf{p} = 2\pi m, \quad m = \pm 1, \pm 2, \dots \quad (7)$$

Although the Berry connection (6) is gauge-dependent [it depends on the local change of phase $\mathcal{A}(\mathbf{p}) \rightarrow e^{i\Phi(\mathbf{p})}\mathcal{A}(\mathbf{p})$ with a continuous function $\Phi(\mathbf{p})$], the winding number m in (7) and the position of the vortex lines are gauge-invariant. Note that one can define the Berry connection directly for the function $\mathcal{A}(\mathbf{p})$. In this case, it represents the analog of the momentum density (or probability current) distribution.

To further investigate the vortices of $\mathcal{A}(\mathbf{p})$, we shall use the concept of the Poincaré section, which in our case is, in principle, an arbitrary plane in the parametric space. We note that such a concept is commonly used in the analysis of quasiperiodic and/or chaotic motion in the classical mechanics [50,51]. However, we extend its definition to interpret our numerical results of phase and modulus of the function $\mathcal{A}(\mathbf{p})$. In doing so, we define a flat two-dimensional section (in the three-dimensional space), where the local properties of this function can be analyzed. This is in contrast to a two-dimensional projection, where local details are blurred due to averaging over the third dimension. Our Poincaré plane is characterized by a unit vector \mathbf{N} perpendicular to it, and by a real number d ($|d|$ represents its distance to the origin of coordinate system). Thus, the equation defining the Poincaré section has the form

$$\mathbf{N} \cdot \mathbf{p} = d. \quad (8)$$

In addition, we introduce two unit vectors, \mathbf{e}_1 and \mathbf{e}_2 , that are perpendicular to \mathbf{N} and together form the right-handed system of vectors, such that $\mathbf{N} = \mathbf{e}_1 \times \mathbf{e}_2$. Then the plane can be defined parametrically as $\mathbf{p}(u, v) = \mathbf{p}_0 + u\mathbf{e}_1 + v\mathbf{e}_2$, where \mathbf{p}_0 determines a specific point on the plane and (u, v) are arbitrary real parameters. In this Poincaré section, while the vortex lines are represented as isolated points, the nodal surfaces are mapped into lines. It may also happen that a 3D vortex line (or parts of it) belongs to the Poincaré section. In such a case, the discrimination between a vortex line and a nodal surface is (in principle) not possible, unless another Poincaré section is chosen (see Appendix). In doing so, the vortex line appears now as an isolated nodal point for which the phase of $\mathcal{A}(\mathbf{p})$ adopts all possible values, modulo 2π , around it.

Let \mathbf{p}_0 define the position of the vortex in the parametric space. Then the contour \mathcal{C} can be chosen as a circle of radius p_r such that $\mathbf{p}(\varphi) = \mathbf{p}_0 + p_r(\cos \varphi \mathbf{e}_1 + \sin \varphi \mathbf{e}_2) \in \mathcal{C}$ for $\varphi \in [0, 2\pi]$. With this choice the circulation around the vortex point \mathbf{p}_0 is equal to

$$\int_0^{2\pi} p_r v_{\parallel}(\varphi) d\varphi = 2\pi m(p_r), \quad (9)$$

where

$$v_{\parallel}(\varphi) = \mathbf{v}(\mathbf{p}(\varphi)) \cdot (-\sin \varphi \mathbf{e}_1 + \cos \varphi \mathbf{e}_2), \quad (10)$$

and the integer function $m(p_r)$ indicates how many vortices (together with their multiplicities) are surrounded by the contour \mathcal{C} .

In closing this section, let us note that, from a mathematical point of view, the concept of vorticity can be introduced for any complex function of two or three variables. However, not all such functions have physical relevance. Below we investigate an example of a function that is related to physical measurements.

IV. PHOTODETACHMENT

Until now our considerations have been general. In the following, we shall apply them to investigate the formation of quantum vortices in photodetachment from the atomic anion H^- .

A. Numerical methods

The theoretical analysis of photodetachment from negatively charged ions offers certain advantages as compared to photoionization from neutral atoms or positive ions. An appropriate description of low-energy photoionization needs to account for the temporal evolution of the electron in the presence of both the laser field and the Coulomb potential. However, in photodetachment, when the emitted electron evolves in the continuum, no interaction with a long-range Coulomb potential is present and the SFA, in its original formulation, is fully justified.

In essence, in the SFA, the exact electron scattering state (which contains information about the interaction with the binding potential and the light field) is approximated by a laser-dressed electron plane wave (the Volkov solution [52]). Such an approximation breaks the gauge invariance of the theory, and, in general, the SFA leads to different predictions when the velocity or length gauges are used. However, as was noticed by Gribakin and Kuchiev [53] and corroborated in Ref. [26], both gauges give the exact same results when, in photodetachment, the unperturbed ground-state wave function is modeled as the bound state of a zero-range potential. This is the case analyzed in the present paper.

In the following, we shall analyze the photodetachment from H^- driven by a linearly polarized laser pulse of duration T_p (see Sec. IV B). The probability amplitude of detachment in the momentum space, $\mathcal{A}(\mathbf{p})$, under the scope of the SFA (length gauge) is given by [26]

$$\mathcal{A}(\mathbf{p}) = ie \int_0^{T_p} dt \mathcal{E}(t) \cdot \tilde{\Phi}_0(\mathbf{p} - e\mathbf{A}(t))e^{iS(\mathbf{p}, t)}, \quad (11)$$

where

$$S(\mathbf{p}, t) = \left[\frac{\mathbf{p}^2}{2m_e} - E_0 \right] t - \frac{1}{m_e} \int_0^t dt' \left[e\mathbf{A}(t') \cdot \mathbf{p} - \frac{e^2 A^2(t')}{2} \right], \quad (12)$$

E_0 is the ground-state energy of the anion, $\mathbf{A}(t)$ is the vector potential defining the laser pulse, whereas $\mathcal{E}(t) = -\partial_t \mathbf{A}(t)$ is the corresponding electric field. Here we have introduced the function

$$\tilde{\Phi}_0(\mathbf{p}) = i\nabla_{\mathbf{p}} \tilde{\Phi}_0(\mathbf{p}), \quad (13)$$

where $\tilde{\Phi}_0(\mathbf{p})$ represents the Fourier transform of the unperturbed ground-state wave function, $\Phi_0(\mathbf{r})$. In our calculations, we chose the latter as the bound state of a zero-range potential (*s*-symmetry) [26,53],

$$\Phi_0(\mathbf{r}) = \Phi_s(\mathbf{r}) = \frac{1}{\sqrt{4\pi a_0}} \frac{A}{r} e^{-\kappa r/a_0}. \quad (14)$$

The constants κ and A are dimensionless and have been set to $A = 0.75$ and $\kappa = 0.2354$. While κ is determined by the ground-state energy $E_0 = -\alpha^2 m_e c^2 \kappa^2 / 2 = -0.754$ eV [26,53], the constant A is, in fact, a fitting parameter that can be adjusted according to the results obtained by different approaches, for instance by solving the TDSE for a model short-range binding potential. To calculate the probability amplitude $\mathcal{A}(\mathbf{p})$ in Eq. (11), we perform the integral over time numerically, i.e., we calculate $\mathcal{A}(\mathbf{p})$ in the length gauge. Although it can be derived also in the velocity gauge, the numerical results arising from both formulations are identical [26].

For the numerical solution of the TDSE, the wave function describing the electron dynamics is calculated at every time step of its evolution. By using the single-active electron approximation and by considering only the velocity gauge (we have checked that our TDSE results are gauge-independent), the full Hamiltonian describing the system is given by

$$H(t) = -\frac{\nabla^2}{2m_e} + V(\mathbf{r}) + i\frac{e}{m_e} \mathbf{A}(t) \cdot \nabla, \quad (15)$$

where $V(\mathbf{r}) = V(r)$ is modeled by the spherically symmetric Yukawa potential,

$$V(r) = -1.1\alpha c \frac{e^{-r/a_0}}{r}. \quad (16)$$

The parameters in (16) have been adjusted such that the ground-state energy is consistent with that arising in the SFA. For our calculations, the electron wave function is expanded using spherical harmonics,

$$\psi(\mathbf{r}, t) = \frac{1}{r} \sum_{l=0}^{l_{\max}} \sum_{m=-l}^l \psi_{lm}(r, t) Y_{lm}(\hat{\mathbf{r}}), \quad (17)$$

where $\hat{\mathbf{r}} = \mathbf{r}/r$ determines the polar and azimuthal angles in the configuration space. The radial coordinate r is discretized by the finite-difference method with a maximum grid point r_{\max} . The Crank-Nicolson propagator is used to determine the wave function evolution from the initial to the final state,

which is then projected onto the scattering state for the static potential (16) to obtain the ionization momentum spectrum. Hence, the probability amplitude of photodetachment, under the scope of the TDSE, can be expressed as follows [54]:

$$\mathcal{A}(\mathbf{p}) = \frac{2\pi}{p} \sum_{l=0}^{l_{\max}} \sum_{m=-l}^l (-i)^l e^{i\delta_l} Y_{lm}(\hat{\mathbf{p}}) \times \int_0^{r_{\max}} dr \psi_{lm}(r, t_f) r R_{pl}(r), \quad (18)$$

where $\hat{\mathbf{p}} = \mathbf{p}/p$ determines the polar and azimuthal angles in momentum space, δ_l is the phase shift, and R_{pl} stands for radial part of the scattering state. According to these definitions, for both the SFA and TDSE, the total photodetachment probability is equal to

$$P_{\text{tot}} = \int \frac{d^3 p}{(2\pi)^3} |\mathcal{A}(\mathbf{p})|^2 = \int \frac{d^3 p}{(2\pi p_0)^3} |p_0^{3/2} \mathcal{A}(\mathbf{p})|^2, \quad (19)$$

where p_0 is the atomic unit of momentum and $p_0^{3/2} \mathcal{A}(\mathbf{p})$ defines the dimensionless momentum distribution or the probability amplitude in atomic units.

To guarantee the convergence of our results from the numerical solution of the TDSE, we have chosen a spatial grid in radial coordinates with $r_{\max} = 1120$ a.u. and grid spacing $\delta_r = 0.01$ a.u. (namely 1.12×10^5 points are used); the maximum azimuthal number in the decomposition (17) is $l_{\max} = 50$. The time step for the temporal evolution is $\delta_t = 0.01$ a.u. Such parameters are used in all our TDSE simulations to obtain convergent results.

B. Laser pulse

For our numerical illustrations, we choose a three-cycle ($N_{\text{osc}} = 3$), linearly polarized laser pulse with a sine-squared envelope. The propagation and polarization directions coincide with the \mathbf{e}_z and \mathbf{e}_x axis, respectively. The electric field defining such a pulse is given by

$$\mathcal{E}(\phi) = F(\phi) \mathbf{e}_x, \quad (20)$$

where

$$F(\phi) = \mathcal{E}_0 \sin^2\left(\frac{\phi}{2}\right) \sin(N_{\text{osc}}\phi + \chi) \quad (21)$$

for $\phi \in [0, 2\pi]$ and 0 outside this interval. Here, $\phi = \omega t$ is the phase of the laser field, $\omega = 2\pi/T_p$, whereas T_p is the pulse duration. Additionally, χ represents the carrier-envelope phase (CEP), $\mathcal{E}_0 = \mathcal{E}_{\text{at}} \sqrt{I/I_0}$ is the amplitude of field oscillations with I being the maximum temporal intensity of the pulse, whereas $I_0 = 7.02 \times 10^{16}$ W/cm² is the atomic unit of intensity. The vector potential associated with this light field is given by

$$\mathbf{A}(\phi) = f(\phi) \mathbf{e}_x, \quad (22)$$

where

$$f(\phi) = -\frac{1}{\omega} \int_0^\phi d\phi' F(\phi'). \quad (23)$$

To estimate approximately the strength of the field-ion interaction, we introduce here the so-called Keldysh parameter

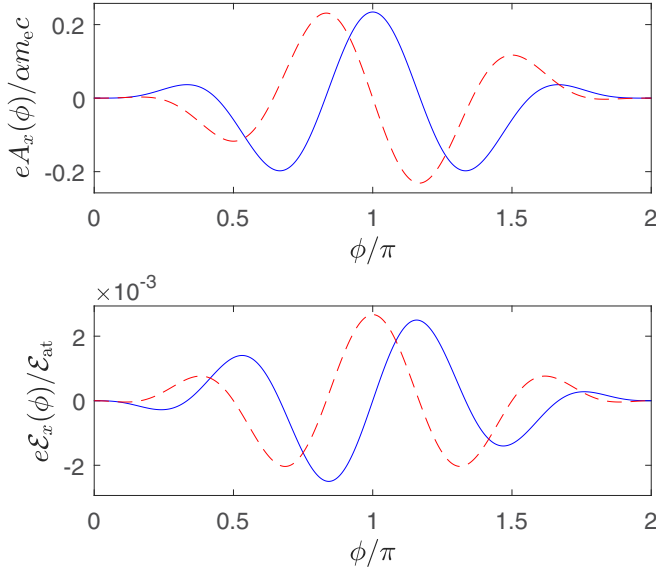


FIG. 1. The vector potential (upper panel) and the electric field (lower panel) as functions of the phase ϕ for the pulse defined by (21). Here, we set $N_{\text{osc}} = 3$, $I = 5 \times 10^{11}$ W/cm 2 , and $\lambda = 4000$ nm. While the solid blue line relates to $\chi = 0$, the dashed red curve is for $\chi = \pi/2$.

[35] $\gamma = \sqrt{|E_0|/2U_p}$, where $U_p = e^2 E_0^2 / (4m_e \omega_L^2)$ is the maximum ponderomotive energy of the electron in the laser field, and $\omega_L = N_{\text{osc}} \omega$ is the laser carrier frequency. The Keldysh parameter will be calculated for the field intensities and frequencies used in this paper.

In Fig. 1 we show the evolution of the x -components of the vector potential multiplied by the electron charge, $eA_x(\phi)$ [Eq. (23), upper panel], and electric field, $eE_x(\phi)$ [Eq. (21), lower panel], as functions of the phase ϕ , for the laser pulse described above. We choose the wavelength $\lambda = 4000$ nm and the peak intensity $I = 5 \times 10^{11}$ W/cm 2 . While the solid blue lines relate to a zero CEP ($\chi = 0$), the dashed red lines are for $\chi = \pi/2$. Note that, for the light fields considered here, both the electric field and the vector potential vanish at $\phi \leq 0$ and $\phi \geq 2\pi$. Since our laser pulses are axially symmetric, the photodetachment amplitude will depend only on two components of momentum: parallel $p_{\parallel} = p_x$ and perpendicular p_{\perp} to the polarization axis. Moreover, the nodal surfaces of the probability amplitude are also axially symmetric, and vortex lines appear as circles with centers located along the e_x axis. Due to this symmetry, we can choose the Poincaré section as the xz -plane. In doing so, the nodal surfaces are seen as symmetric lines with respect to the polarization axis, and vortex lines appear as two single points located at $(p_x, \pm p_z)$. If for the vortex point (p_x, p_z) the topological charge is m , then for its twin point $(p_x, -p_z)$ it has to be $-m$, as both of them belong to the same closed vortex line.

V. NUMERICAL ANALYSIS

To analyze the formation of vortices in photodetachment, we present the magnitude and the phase of the probability amplitude, $\mathcal{A}(\mathbf{p})$, for the driving field described above. Our results have been obtained within the SFA theory [Eq. (11)]

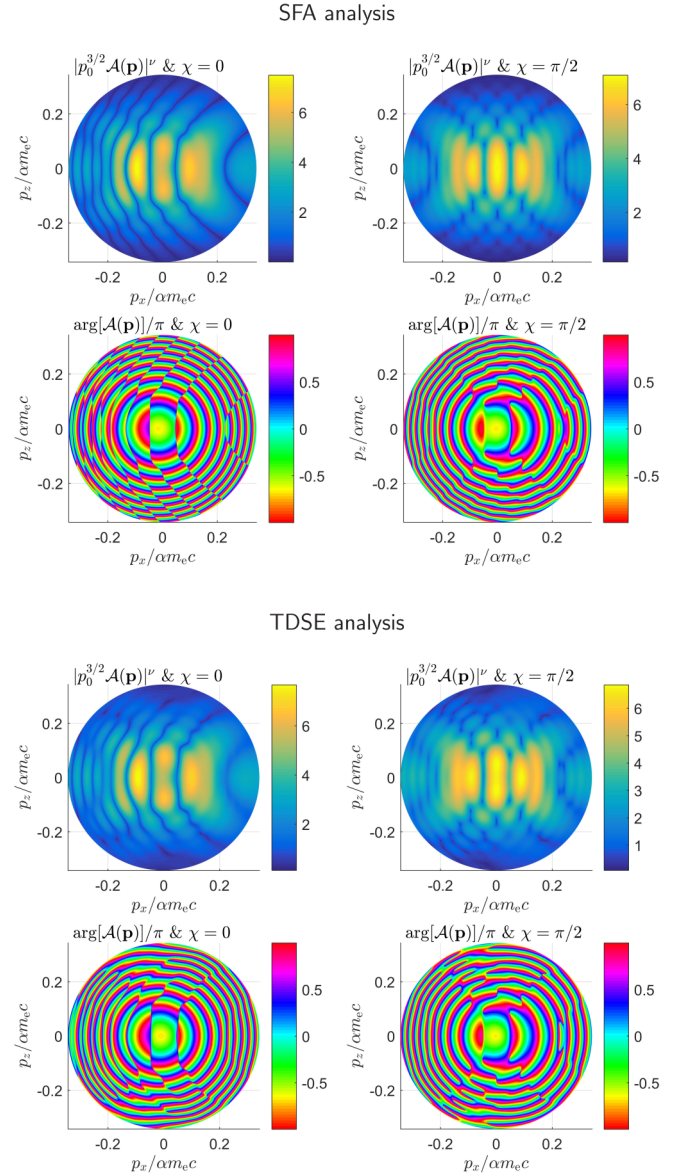


FIG. 2. Color mappings of the magnitude of the dimensionless probability amplitude of detachment $|p_0^{3/2} \mathcal{A}(\mathbf{p})|^\nu$ (where $p_0 = \alpha m_e c$ is the atomic unit of momentum and $\nu = 0.5$ has been chosen for visual purposes), and its phase $\arg[\mathcal{A}(\mathbf{p})]$ for a three-cycle laser pulse of wavelength $\lambda = 4000$ nm, peak intensity $I = 5 \times 10^{11}$ W/cm 2 , with CEP of either $\chi = 0$ (left panels) or $\chi = \pi/2$ (right panels). The strength of field oscillations is $\mathcal{E}_0 = 2.7 \times 10^{-3}$ a.u. and the Keldysh parameter is $\gamma \approx 1.0$. While the upper part of this figure corresponds to the SFA results [Eq. (11)], the lower part corresponds to the TDSE results [Eq. (18)]. The Poincaré section coincides with the $p_x p_z$ -plane, i.e., we set $p_y = 0$.

as well as from solving the TDSE [Eq. (18)]. The objective here is to investigate the role of the CEP, laser field intensity, and pulse duration in the formation of vortex structures in the resulting electron momentum distributions.

A. CEP effects

In the upper part of Fig. 2 (labeled as ‘‘SFA analysis’’), we show the results obtained from the SFA formalism [Eq. (11)].

We present the magnitude of the probability amplitude of detachment raised to the power $\nu = 0.5$ (for visual purposes), $|p_0^{3/2}\mathcal{A}(\mathbf{p})|^\nu$, and its phase, $\arg[\mathcal{A}(\mathbf{p})]$. The Poincaré section coincides with the $p_x p_z$ -plane (i.e., we set $p_y = 0$). The parameters of the driving laser field have been introduced in Sec. IV B. While the CEP in the left panels is zero, in the right panels it is $\pi/2$. From the upper left panel we see that, for $\chi = 0$, no isolated nodes are present in the Poincaré section, meaning that only nodal surfaces exist in the 3D momentum space. Furthermore, by inspecting the phase of the probability amplitude (lower left panel, SFA analysis) we conclude that no vortex structures are formed, as $\arg[\mathcal{A}(\mathbf{p})]$ jumps by π while crossing a nodal surface. From the upper right panel of the SFA calculations ($\chi = \pi/2$) we observe the formation of a honeycomb-like structure in the momentum distribution of photoelectrons; hexagonal zones of large probability are surrounded by lines of low probability, with nodes found at some of its vertices. By looking at the phase (lower right panel, SFA analysis) one can see the presence of actual vortex lines. The latter are identified as isolated nodes in our Poincaré section, with the phase changing from 0 to 2π around them. In particular, at low photoelectron energies ($p_r = \sqrt{p_x^2 + p_z^2} < 0.2\alpha m_e c$) vortices with topological charge $m > 0$ and their antivortices (with topological charge $-m$) are observed. However, at larger energies they merge together, which leads to their mutual annihilation (as will be discussed in Sec. V D).

Next, we compare the results obtained from the SFA and the direct numerical solution of the TDSE. For this purpose, in the lower part of Fig. 2 (labeled as ‘‘TDSE analysis’’) we present the results for the probability amplitude of detachment calculated from the TDSE [Eq. (18)]. We find that the results from both treatments agree well with each other. Nevertheless, there are certain differences that stand out. For instance, for a vanishing carrier-envelope phase ($\chi = 0$) the SFA predicts the formation of well-defined nonvortex nodal surfaces across the whole range of momentum considered here. However, the TDSE shows a not so well-defined series of lines located at very similar positions in the Poincaré section (see the left panels of Fig. 2). This may be caused by the rescattering effects present in the TDSE. For $\chi = \pi/2$, the TDSE predicts the formation of the same honeycomb patterns analyzed above with vortices and antivortices located at some of the corners of the hexagonal patterns (see the right panels of Fig. 2). Note that now the symmetry $p_x \rightarrow -p_x$ is broken, which again can be attributed to the rescattering effects. Despite these differences, the overall agreement between TDSE and SFA is very good.

As has already been discussed in Ref. [34], the origin of nodal surfaces and vortex lines is due to the interference of probability amplitudes leading to the same final state of a given momentum, but by different intermediate states (in fact, this is the common interpretation of vortex structures observed not only in quantum physics, but also in classical electrodynamics and optics [11]). As such, the interference pattern is very sensitive to changes of external forces. For $\chi = 0$, in the SFA we observe only nodal surfaces. As we have checked, this happens because some of the nodal surfaces of the real and imaginary parts of $\mathcal{A}(\mathbf{p})$ coincide. These particular nodal surfaces are gauge-invariant, as their positions

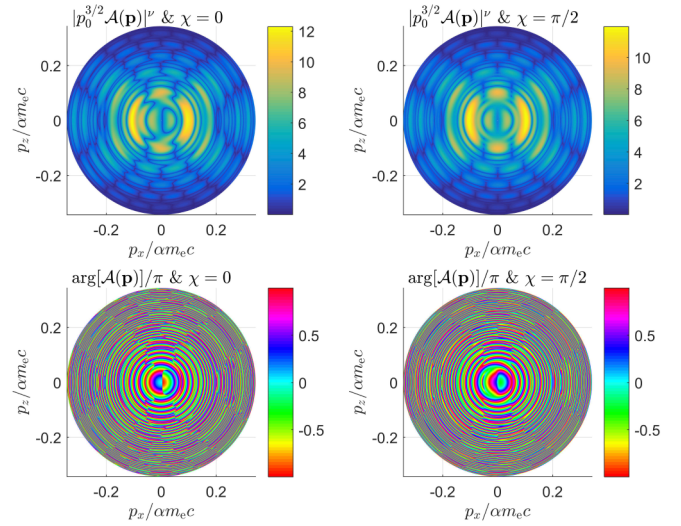


FIG. 3. The same as in the upper part of Fig. 2 (SFA analysis) but for a 13-cycle laser pulse. Again, the field strength is $\mathcal{E}_0 = 2.7 \times 10^{-3}$ a.u. and the Keldysh parameter is $\gamma \approx 1.0$.

and shapes are independent of a momentum-dependent phase factor that multiplies the amplitude (the same concerns the vortex lines). The presence of a nodal surface of the complex amplitude is exceptional. Namely, with small changes of the laser pulse parameters, the real and imaginary nodal surfaces change their shapes, and instead of common surfaces, we either obtain vortex lines at their intersections, or the zeros of probability amplitude completely disappear. In particular, the change of CEP can lead to such effects. Our numerical analysis shows that the vortex lines emerge for all CEP except 0 and π . On the other hand, for a shorter pulse of $N_{\text{osc}} = 2$, the gauge-invariant nodal surfaces also exist only for $\chi = 0$ or π . For all other values of CEP, the amplitude $\mathcal{A}(\mathbf{p})$ does not exhibit any zeros. This raises another question: Do vortices exist for longer pulses? This problem is considered in the next section.

B. Pulse duration (N_{osc}) effects

Up to now, we have seen that the CEP plays a fundamental role in the control of vortex structures in photodetachment driven by short laser pulses. However, it would be interesting to explore the effect of pulse duration as well. As both the SFA and the TDSE lead to very similar results, in the following we shall only present the numerical calculations based on the SFA [i.e., the probability amplitude of detachment is obtained from Eq. (11)]. In Fig. 3, we show the magnitude of the probability amplitude, raised to the power $\nu = 0.5$, and its phase for the laser pulse (21) comprised of $N_{\text{osc}} = 13$ oscillations. The laser peak intensity and wavelength are still the same (namely, $I = 5 \times 10^{11}$ W/cm² and $\lambda = 4000$ nm, respectively). We also choose the same Poincaré section ($p_x p_z$ -plane). Our results are presented for $\chi = 0$ (left panels) and $\chi = \pi/2$ (right panels). For $\chi = 0$, we observe the presence of multiple nodal surfaces (lines of zero probability along our chosen plane) and no nodal lines (no isolated points of vanishing probability). From the amplitude’s phase (lower-left panel), we conclude that no vortices are formed when the CEP vanishes. However,

for $\chi = \pi/2$ both nodal surfaces and nodal lines are present (upper-right panel) and new pairs of vortices and antivortices are created (lower-right panel). Note, however, that the color maps shown in the left and right panels of Fig. 3 are rather similar. This supports the commonly accepted assumption that, for long pulses, the CEP does not play a significant role in the ionization or detachment dynamics. Nevertheless, we observe densely distributed vortices in our numerical results for $\chi = \pi/2$. In fact, had our figures had a smaller resolution, the vortex lines would not have been distinguished from simple nonvortex nodal lines. For this reason it would be difficult (if not impossible) to observe the differences created by a CEP in experimental setups. This is another example that shows that for very short pulses some seemingly hidden properties of the ionization distributions can be displayed or revealed in a more transparent form.

Ultrashort laser pulses (few cycles) are characterized by a very broad frequency spectrum. Therefore, it becomes questionable to ascribe a definite number of photons to the detachment process for small N_{osc} . Nevertheless, for a pulse comprising 13 cycles within the \sin^2 envelope, one can approximate the number of photons necessary to detach the electron. For the laser field considered in this section ($N_{\text{osc}} = 13$ and $\lambda = 4000$ nm), we assume that each light quanta has an energy $\omega_L \approx 0.31$ eV. For the ionic target H^- the electron affinity is $|E_0| = 0.754$ eV, hence at least three photons are necessary to promote the outermost electron to the continuum. This is in contrast to the analysis developed in Ref. [34], where it is assumed that the carrier frequency of the driving field is larger than the absolute value of the binding energy.

C. Intensity effects

We consider the photodetachment from H^- by a laser pulse that is ten times more intense as compared to the one shown in Fig. 1. Namely, we set now the peak intensity $I = 5 \times 10^{12}$ W/cm² while keeping the same number of field oscillations ($N_{\text{osc}} = 3$) and wavelength ($\lambda = 4000$ nm). The magnitude (raised to the power $\nu = 0.5$) and phase of the probability amplitude of detachment, $\mathcal{A}(\mathbf{p})$ [Eq. (11)], are shown in the upper and lower panels of Fig. 4, respectively. The Poincaré section is the $p_x p_z$ -plane, and we present our simulations for the CEPs: $\chi = 0$ (left panels) and $\chi = \pi/2$ (right panels). While for $\chi = 0$ only nodal surfaces appear in the momentum distribution, for $\chi = \pi/2$ a rich combination of nodal surfaces and nodal lines can be observed. Furthermore, in the latter case, the probability distribution exhibits a characteristic honeycomb pattern (upper-right panel) with vortices at the corners of each hexagon (lower-right panel). In comparison to the case shown in the right panels of Fig. 2 (SFA analysis), obtained at a lower field intensity, the hexagonal regions of large probability are now denser and better defined, whereas vortices are observed at larger photoelectron energies. In fact, as will be shown in the next section, pairs of vortices and antivortices are observed in this probability distribution.

D. Vortex-antivortex creation and/or annihilation

To analyze the formation or annihilation of vortices, in Fig. 5 we present the same as in Fig. 4 but this time the

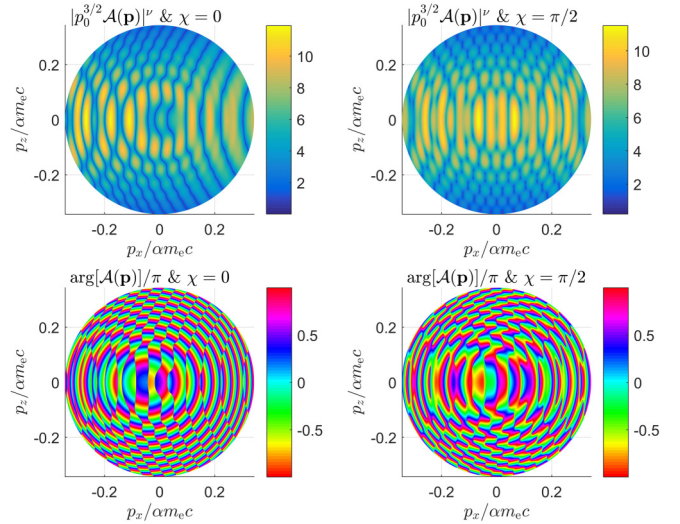


FIG. 4. The same as in the upper part of Fig. 2 (SFA analysis) but for the laser pulse peak intensity $I = 5 \times 10^{12}$ W/cm². The magnitude of the probability amplitude (upper panels) is raised to the power $\nu = 0.5$. Now, the strength of field oscillations is $\mathcal{E}_0 = 8.4 \times 10^{-3}$ a.u. and the Keldysh parameter is $\gamma \approx 0.32$.

Poincaré section ($p_x p_z$ -plane) is defined in polar coordinates ($p_x = p_r \cos \varphi$ and $p_z = p_r \sin \varphi$). Our results here are shown for a more narrow range of momenta p_r and polar angles φ as compared to Fig. 4, such that the fine details can be observed. It can be seen that, for $\chi = 0$, the phase of the probability amplitude jumps by π while crossing a nodal surface (lower-left panel of Fig. 5). For $\chi = \pi/2$, such a nodal surface (visualized as a line in our Poincaré section) splits into the

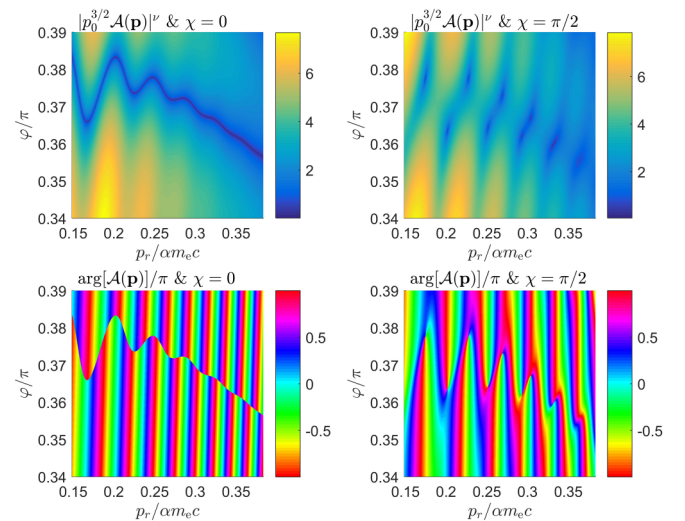


FIG. 5. The same as in Fig. 4 but for a Poincaré section ($p_x p_z$ -plane) in polar coordinates (see the text). The magnitude of the probability amplitude (upper panels) is raised to the power $\nu = 0.5$. For $\chi = \pi/2$ the nodal surface splits into the von Kármán street of vortices and antivortices. With increasing the radial momentum p_r , vortices and antivortices approach each other, leading to their annihilation. Hence, for sufficiently large energies of photoelectrons no vortex structures are observed.

von Kármán street of vortices and antivortices. The separation between them decreases with increasing $p_r = \sqrt{p_x^2 + p_z^2}$. The behavior of the phase around them (see the lower-right panel of Fig. 5) indicates that the pair of vortices rotates in opposite directions, i.e., they are characterized by opposite winding numbers $m = \pm 1$. Moreover, for sufficiently large momentum they annihilate each other and the vortex structure disappears. The annihilation process is represented by the connection of vertical green (light gray) ribbons, as shown in the lower-right panel of Fig. 5. In this context, it can be said that vortices and antivortices behave somehow as particle-antiparticle pairs, with the topological charge taking the place of the electric charge. Namely, when they encounter each other, mutual annihilation leads to the disappearance of vorticity.

VI. CONCLUSIONS

We have analyzed the formation of vortex structures in photodetachment of the H^- anion driven by linearly polarized laser pulses. According to our numerical simulations, zero CEPs (modulo π) lead to momentum distributions characterized by multiple nodal surfaces and no vortices in the SFA. In contrast, for nonvanishing CEPs, both nodal surfaces and vortex lines are present, leading to von Kármán-type streets of vortices. Furthermore, for $\chi = \pi/2$ the spectra of photoelectrons exhibit hexagonal zones of high probability. Those zones form a honeycomb structure with pairs of vortices and antivortices located at the corners of the hexagons. Such pairs annihilate each other at large photoelectron energies. Even though our theoretical analysis predicts the formation of vortices for long driving pulses, we do not expect them to be easily seen in realistic experimental setups. This is due to the finite resolution inherent to them. One can also anticipate from our investigations that the favorite conditions for observing vortex structures (such as von Kármán streets or honeycomb patterns) are met for few-cycle pulses, at least for the symmetric envelopes considered here. One can expect that these vortex structures can significantly be changed if asymmetric envelopes or bichromatic pulses are applied. Investigation of such possibilities is, however, beyond the scope of the present paper.

In conclusion, we have shown that linearly polarized pulses can generate vortical structures in photodetachment. An active control of the CEP can be used to modify the vortex structures of the resulting photoelectron momentum distributions. Consequently, as the probability distribution of photoelectrons in the momentum space is sensitive to the parameters defining the light field, it could be possible to develop novel diagnostic techniques. In principle, one could determine the carrier-envelope phase and intensity of the laser pulse by inspecting the location of vortices in a given Poincaré section. This is provided that the driving pulse is sufficiently short.

ACKNOWLEDGMENTS

This work is supported by the National Science Centre (Poland) under Grants No. 2018/31/B/ST2/01251 (F.C.V.) and No. 2018/30/Q/ST2/00236 (J.Z.K. and K.K.), and by the National Natural Science Foundation of China (NSFC) under Grants No. 11961131008 and No. 11725416 and by

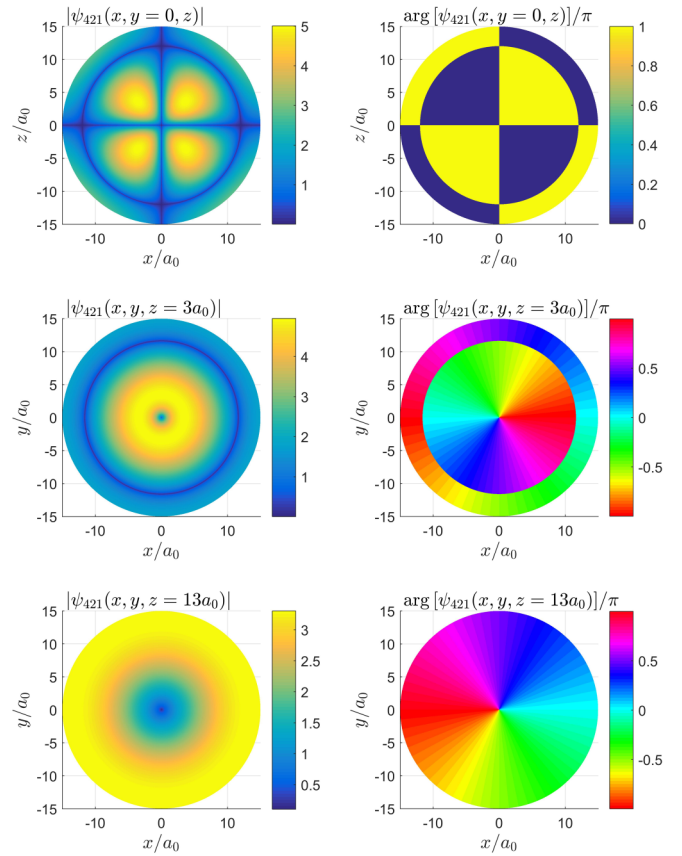


FIG. 6. Magnitude (left column) and phase (right column) of the wave function $\psi_{421}(x, y, z)$ [see Eq. (A1)] for the Poincaré planes $y = 0$ (upper row), $z = 3a_0$ (middle row), and $z = 13a_0$ (lower row).

the National Key R&D Program of China under Grant No. 2018YFA0306302 (L.G. and L.P.).

F.C.V. and L.G. contributed equally to this work.

APPENDIX: NODAL SURFACES AND VORTEX LINES

To illustrate the formation of nodal surfaces and vortex lines, we take as an example the bound state of a hydrogen atom in spherical coordinates. Namely, we choose the wave function corresponding to the principal quantum number $n = 4$, angular number $\ell = 2$, and magnetic quantum number $m = 1$. In this case, the wave function (up to the normalization constant) equals

$$\begin{aligned} \psi_{421}(x, y, z) &= \left(\frac{r}{a_0}\right)^2 \left(\frac{r}{a_0} - 12\right) e^{-r/4a_0} \cos\theta \sin\theta e^{i\varphi} \\ &= \left(\frac{r}{a_0} - 12\right) \frac{z(x + iy)}{a_0^2} e^{-r/4a_0}, \end{aligned} \quad (\text{A1})$$

where $r = \sqrt{x^2 + y^2 + z^2}$. The bound state (A1) has two nodal surfaces: a plane located at $z = 0$ and a spherical surface of radius $r = 12a_0$ centered at the coordinates origin. Additionally, there is a vortex line with topological charge $m = 1$ located at $x = y = 0$. This is shown in Fig. 6, where we present the magnitude (left column) and phase (right column) of $\psi_{421}(x, y, z)$ for the Poincaré planes $y = 0$ (upper row), $z = 3a_0$ (middle row), and $z = 13a_0$ (lower row). In the

upper left panel, we observe the spherical nodal surface as an annular region of zero probability; the nodal plane appears as a horizontal line located at $z = 0$ while the vortex line, which lies in this section, can be identified as the vertical line ($x = 0$). From the upper right panel we see that, by traversing the nodal surfaces or the vortex line (topological charge $m = 1$), the phase of the wave function changes by π . It is clear that this choice of a Poincaré section does not allow us to distinguish between nodes and vortices. For this reason, we use now the Poincaré plane $z = 3a_0$ (middle row of the same figure). As expected, the nodal sphere is now seen as a ring of radius $\sqrt{135}a_0 \approx 11.6a_0$ and the phase of the wave function changes by π while crossing it. This time, the vortex line intersects our section at $x = y = 0$ and appears as a point of zero probability at the origin of coordinates; the phase of the wave function changes continuously from 0 to 2π around it. Moreover, as $z = 3a_0 > 0$, the nodal plane is not visible.

Finally, for the Poincaré section $z = 13a_0$ (lower row) we only observe the presence of the vortex line as $z > 12a_0$, i.e., the plane is located at a distance from the origin of coordinates larger than the radius of the nodal sphere. Note that a very similar pattern is observed in the momentum space, as the wave function is proportional to

$$\tilde{\psi}_{421}(\mathbf{p}) = \frac{(4p/p_0)^2 - 1}{[(4p/p_0)^2 + 1]^5} \frac{p_z(p_x + ip_y)}{p_0^2}, \quad (\text{A2})$$

where $p = \sqrt{p_x^2 + p_y^2 + p_z^2}$.

In conclusion, we have shown here that nodal surfaces and lines are mapped into lines or points of zero probability in a given Poincaré section. We also highlighted the importance of a properly chosen Poincaré plane in order to distinguish between nodes and vortices.

-
- [1] *Spirals and Vortices in Culture, Nature, and Science*, edited by K. Tsuji and S. C. Müller (Springer, Cham, 2019).
- [2] H. von Helmholtz, *Philos. Mag.* **33**, 485 (1867).
- [3] W. Thomson, *Philos. Mag.* **34**, 15 (1867).
- [4] S. J. Putterman, *Superfluid Hydrodynamics* (Elsevier, New York, 1974).
- [5] D. R. Tilley and J. Tilley, *Superfluidity and Superconductivity* (Van Nostrand Reinhold, New York, 1974).
- [6] H. Saarikoski, S. M. Reimann, A. Harju, and M. Manninen, *Rev. Mod. Phys.* **82**, 2785 (2010).
- [7] P. McCormack, *Vortex, Molecular Spin and Nanovorticity* (Springer, New York, 2012).
- [8] I. Carusotto and C. Ciuti, *Rev. Mod. Phys.* **85**, 299 (2013).
- [9] K. Y. Bliokh, I. P. Ivanov, G. Guzzinati, L. Clark, R. Van Boxem, A. Béch e, R. Juchtmans, M. A. Alonso, P. Schattschneider, F. Nori, and J. Verbeeck, *Phys. Rep.* **690**, 1 (2017).
- [10] S. M. Lloyd, M. Babiker, G. Thirunavukkarasu, and J. Yuan, *Rev. Mod. Phys.* **89**, 035004 (2017).
- [11] A. J. Taylor, *Analysis of Quantised Vortex Tangle* (Springer, Cham, 2017).
- [12] C. Rosales-Guzm an, B. Ndagano, and A. Forbes, *J. Opt.* **20**, 123001 (2018).
- [13] M. Babiker, D. L. Andrews, and V. E. Lembessis, *J. Opt.* **21**, 013001 (2019).
- [14] R. B. Laughlin, *Phys. Rev. Lett.* **50**, 1395 (1983).
- [15] G. E. Volovik, *Pis'ma Zh. Eksp. Teor. Fiz.* **52**, 972 (1990) [*JETP Lett.* **52**, 358 (1990)].
- [16] I. Białynicki-Birula, Z. Białynicka-Birula, and C. Śliwa, *Phys. Rev. A* **61**, 032110 (2000).
- [17] S. I. Shevchenko, *Phys. Rev. B* **67**, 214515 (2003).
- [18] K. Krajewska and J. Z. Kamiński, *Phys. Rev. B* **68**, 064418 (2003).
- [19] K. Krajewska, J. Z. Kamiński, and R. M. Potvliege, *Ann. Phys.* **323**, 2639 (2008).
- [20] B. Xu, M. V. Milošević, S.-H. Lin, F. M. Peeters, and B. Jankó, *Phys. Rev. Lett.* **107**, 057002 (2011).
- [21] E. Karimi, L. Marrucci, V. Grillo, and E. Santamato, *Phys. Rev. Lett.* **108**, 044801 (2012).
- [22] A. Béch e, R. Van Boxem, G. Van Tendeloo, and J. Verbeeck, *Nat. Phys.* **10**, 26 (2014).
- [23] D. Velasco-Mart inez, V. G. Ibarra-Sierra, J. C. Sandoval-Santana, J. L. Cardoso, and A. Kunold, *Phys. Rev. A* **94**, 063815 (2016).
- [24] A. Rajabi and J. Berakdar, *Phys. Rev. A* **95**, 063812 (2017).
- [25] F. Cajiao V elez, K. Krajewska, and J. Z. Kamiński, *Phys. Rev. A* **97**, 043421 (2018).
- [26] F. Cajiao V elez, J. Z. Kamiński, and K. Krajewska, *Phys. Rev. A* **101**, 053430 (2020).
- [27] D. J. Acheson, *Elementary Fluid Dynamics* (Oxford University Press, Oxford, 1990).
- [28] K. Sasaki, N. Suzuki, and H. Saito, *Phys. Rev. Lett.* **104**, 150404 (2010).
- [29] W. J. Kwon, G. Moon, J.-Y. Choi, S. W. Seo, and Y.-I. Shin, *Phys. Rev. A* **90**, 063627 (2014).
- [30] G. W. Stagg, A. J. Allen, C. F. Barenghi, and N. G. Parker, *J. Phys.: Conf. Ser.* **594**, 012044 (2015).
- [31] E. Madelung, *Z. Phys.* **40**, 322 (1926).
- [32] I. Białynicki-Birula, M. Cieplak, and J. Kamiński, *Theory of Quanta* (Oxford University Press, New York, 1992).
- [33] O. I. Tolstikhin and T. Morishita, *Phys. Rev. A* **99**, 063415 (2019).
- [34] N. V. Larionov, S. Yu. Ovchinnikov, A. A. Smirnovsky, and A. A. Schmidt, *Tech. Phys.* **63**, 1569 (2018).
- [35] L. V. Keldysh, *Zh. Eksp. Teor. Fiz.* **47**, 1945 (1964) [*Sov. Phys. JETP* **20**, 1307 (1965)].
- [36] F. H. M. Faisal, *J. Phys. B* **6**, L89 (1973).
- [37] H. R. Reiss, *Phys. Rev. A* **22**, 1786 (1980).
- [38] P. A. M. Dirac, *Proc. R. Soc. London, Ser. A* **133**, 60 (1931).
- [39] J. O. Hirschfelder and A. C. Christoph, *J. Chem. Phys.* **61**, 5435 (1974).
- [40] K. Krajewska, F. Cajiao V elez, and J. Z. Kamiński, *J. Phys.: Conf. Ser.* **1206**, 012002 (2019).
- [41] A. S. Sanz, F. Borondo, and S. Miret-Art es, *Phys. Rev. B* **69**, 115413 (2004).
- [42] C.-C. Chou, A. S. Sanz, S. Miret-Art es, and R. E. Wyatt, *Phys. Rev. Lett.* **102**, 250401 (2009).

- [43] C.-C. Chou, A. S. Sanz, S. Miret-Artés, and R. E. Wyatt, *Ann. Phys.* **325**, 2193 (2010).
- [44] A. S. Sanz and S. Miret-Artés, *Phys. Rep.* **451**, 37 (2007).
- [45] M. V. Berry, *Proc. R. Soc. Lond. A* **392**, 45 (1984).
- [46] W. Dittrich and M. Reuter, *Classical and Quantum Dynamics. From Classical Paths to Path Integrals* (Springer, Berlin, 2001).
- [47] D. Xiao, M.-C. Chang, and Q. Niu, *Rev. Mod. Phys.* **82**, 1959 (2010).
- [48] S. A. H. Gangaraj, M. G. Silveirinha, and G. W. Hanson, *IEEE J. Multiscale Multiphys. Comput. Tech.* **2**, 3 (2017).
- [49] O. Passon, *Entropy* **20**, 440 (2018).
- [50] H. G. Schuster, *Deterministic Chaos. An Introduction* (Physik-Verlag, Weinheim, 1984).
- [51] J. V. José and E. J. Saletan, *Classical Dynamics. A Contemporary Approach* (Cambridge, New York, 1998).
- [52] D. M. Wolkow, *Z. Phys.* **94**, 250 (1935).
- [53] G. F. Gribakin and M. Yu. Kuchiev, *Phys. Rev. A* **55**, 3760 (1997).
- [54] A. F. Starace, Theory of Atomic Photoionization, in *Handbuch der Physik*, edited by W. Mehlhorn (Springer, Berlin, 1982), Vol. 31, pp. 1–121.